

Direct Numerical Simulation of Wall Turbulence with Bubbles

Takafumi Kawamura, Yoshiaki Kodama

Ship Research Institute

A new computational method for investigating interactions between bubbles and turbulence has been developed. Both liquid and gas phases are treated as incompressible continuum fluids and solved by a finite volume method, while the interface between the phases is resolved by a front-tracking method. The accuracy of the method is validated for the problem of a single rising bubble. The method has been applied to a direct numerical simulation (DNS) of a fully developed turbulent channel flow containing bubbles, and some preliminary results have been obtained.

1. Introduction

About 80% of the total propulsion resistance of a ship like a tanker is due to friction with the surrounding water. It will be a great contribution to the environment to reduce the fuel consumption of ships as a means of mass transportation by reducing the frictional drag. There are several devices for reducing the frictional resistance such as passive type devices like riblets or active type devices like the combination of micro sensors and actuators. Among these methods, we consider the microbubble injection method is most suitable for ships.

There is relatively large extent of literature on the microbubble drag reduction. McCormick et al.¹⁾ found that the drag of a submerged body was reduced by microbubbles produced by electrolysis. Madavan et al.²⁾ investigated the relation between the drag reduction and the mean void ratio for a developing turbulent boundary layer on a flat plate. Guin et al.³⁾ experimentally showed that the drag reduction is better correlated with the void fraction near the wall than the mean value. Takahashi et al.⁴⁾ investigated the microbubble drag reduction for a fully developed turbulent boundary layer in a channel.

The drag reduction rate for given amount of microbubbles must be improved in order to make the microbubble drag reduction method fit for practical use. For this purpose, it is important to understand the mechanism of the microbubble drag reduction. Decrease in the mean density, increase in the effective viscosity, and modulation of turbulence are assumed to be responsible. However, convincing answers are still missing.

For developing an advanced model to explain and predict the microbubble drag reduction, more detailed experimental data is needed. However, since the presence of microbubbles strongly hinders measurements by LDV or PIV, the numerical simulation is expected to be an effective alternative approach.

In this study we aim at obtaining a detailed data of the velocity field of turbulent flow modified by

microbubbles.

Two-phase flow simulation methods are classified into three categories. The first way is to solve phase-averaged equations of fluid motion, and the second way is to model bubbles by point force distributions. These approaches are valid for predicting macroscopic feature of the flow, or in particular cases when the size of bubbles can be assumed infinitely small. The third way is to simulate the two-phase flow directly with implementing the continuity of mass and momentum across the air-water interface. Fig. 1 shows a snap photo of the flow dealt with in this study. It is noted that the size of bubbles is relatively large, and the effect of the deformation of bubbles is supposed to be significant. Therefore, we adopt a direct numerical simulation method. Kanai and Miyata⁵⁾ carried out a direct numerical simulation of turbulent Couette flow containing bubbles by use of the marker density method. We apply a similar computational method to a fully developed turbulent channel flow containing bubbles.

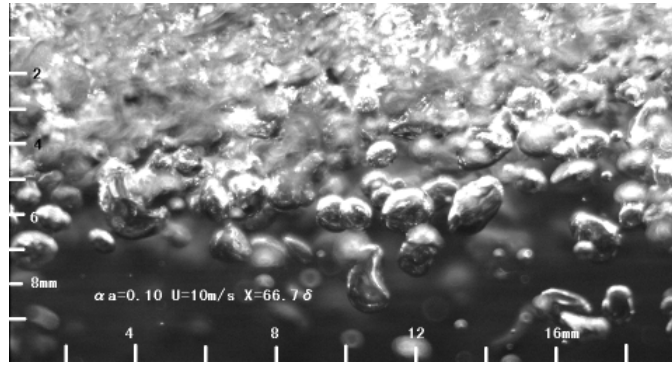


Fig 1. Photograph of bubbles in the channel⁴⁾

2. Numerical Method

2.1 Governing Equations

Both water and air phases are treated as incompressible fluids, and the continuity of stress is implemented at the interface. The governing equations for each phase is the Navier-Stokes equation,

$$\frac{\partial u_i}{\partial t} = -\frac{\partial u_i u_j}{\partial x_j} + \frac{\partial}{\partial x_j} \left\{ \nu \left(\frac{\partial u_i}{\partial x_j} + \frac{\partial u_j}{\partial x_i} \right) \right\} - \frac{1}{\rho} \frac{\partial p}{\partial x_i} \quad (1)$$

and the continuity equation

$$\frac{\partial u_i}{\partial x_i} = 0 \quad (2)$$

where x_i , u_i , and p are the Cartesian coordinate, the velocity components, and static pressure respectively. The fluid density ρ and the kinematic viscosity ν take values of either water or air depending on whether the center of the computational cell is water or air.

2.2 Interface Tracking Method

There are several methods for expressing the moving interface between two fluids, such as the VOF method, the level-set method, and the front-tracking method. The VOF and level-set methods are categorized as the front capturing methods which track the movement of volume and find the interface in an indirect way. One of the merits of the methods of this type is that collision and breakup of interfaces are easily treated. On the other hand, the front-tracking method tracks the interface directly allowing more accurate calculation of the curvature of the interface, although treatment of surface re-structuring is complicated. We use the front-tracking method, since accurate calculation of the interface curvature is very important for the case investigated in this study.

Each bubble is expressed by its center position and radius distribution around the center as shown in Fig 2. Marker particles are placed on each bubble regularly on a two-dimensional spherical grid (θ, φ) . In the beginning of each time step, the positions of the marker particles are updated using the velocity interpolated from the rectangular grid for solving the Navier-Stokes equations. After the marker particles are moved, the radius at each point $r(\theta, \varphi)$ is calculated and expanded in a series of spherical harmonic function,

$$r(\theta, \varphi) = \sum_{n=0}^N \sum_{m=0}^n \{A_{nm} \cos m\varphi + B_{nm} \sin m\varphi\} P_{nm}(\cos\theta) \quad (3)$$

in which N is the number of the deformation modes considered, P_{nm} is Legendre associate polynomial. N is set to 8 in this study. The coefficients A_{nm} and B_{nm} are obtained as follows:

$$A_{n0} = \frac{2n+1}{4\pi} \int_{-\pi}^{\pi} \int_0^{\pi} r(\theta, \varphi) P_{n0}(\cos\theta) \sin\theta d\theta d\varphi \quad (4)$$

$$B_{n0} = 0 \quad (5)$$

$$A_{nm} = \frac{2n+1}{2\pi} \frac{(n-m)!}{(n+m)!} \int_{-\pi}^{\pi} \int_0^{\pi} r(\theta, \varphi) \cos m\varphi P_{nm}(\cos\theta) \sin\theta d\theta d\varphi \quad (6)$$

$$B_{nm} = \frac{2n+1}{2\pi} \frac{(n-m)!}{(n+m)!} \int_{-\pi}^{\pi} \int_0^{\pi} r(\theta, \varphi) \sin m\varphi P_{nm}(\cos\theta) \sin\theta d\theta d\varphi. \quad (7)$$

The primary merit of this method is that the curvature of the interface is accurately computed with relatively small number of grid points. Another advantage is that deformations of high wave number modes, which give rise to numerical instabilities, can be filtered out. Whereas the shortcomings are that the radius must be a single-valued function of the altitude and latitude. Therefore, this method cannot deal with deformations beyond a certain limit, collision or separation of bubbles.

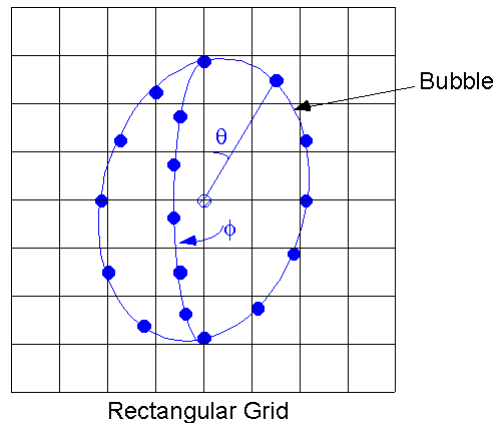


Fig 2. Schematic sketch of the present front-tracking method

2.3 Solution Algorithm

A second-order finite volume method is used for the spatial discretization on a rectangular grid system fixed to the space, and a second-order semi-implicit fractional step method is used for the time integration. At the beginning of each time step, the positions and shapes of bubbles are determined, and the values of density and the kinematic viscosity in each cell are set to values of water or air. Whether a cell-center point is inside a bubble or not can be judged from Equation (3). Then the dynamic boundary condition is set in cells containing interfaces. The surface tension is treated as a pressure jump across the interface. The curvature of the interface is calculated from the expression (3) analytically. Using this interface boundary condition the momentum equations (1) are semi-implicitly integrated, and then corrected by solving a Poisson equation for the pressure. The Poisson equation for the pressure is solved by a multigrid method.

3. Single Rising Bubble

The accuracy of the computational method is examined for the problem of a single bubble rising in quiescent water. Computations are carried out using $64 \times 64 \times 64$ cells for a domain of 4 diameters cube, which moves with the center of the bubble. Fig.3 shows a comparison of the computed drag coefficient C_d and an empirical formula proposed by Tomiyama et al.⁶⁾. Bubbles smaller than 1 mm are almost spherical and rise straight up, while larger bubbles are deformed and show non-axisymmetric swing motions. Computations reproduce this behavior very well, and the calculated C_d values are in good agreement with the empirical formula. Fig 4 shows computed ellipsoidal shape of the bubble. The flatness is confirmed to be also in good agreement with experiments.

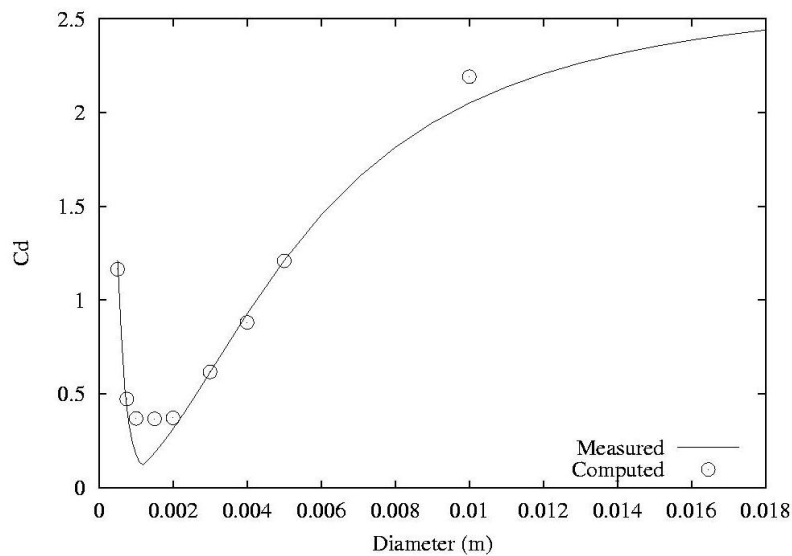


Fig 3. Drag coefficient of a single rising bubble in clean water

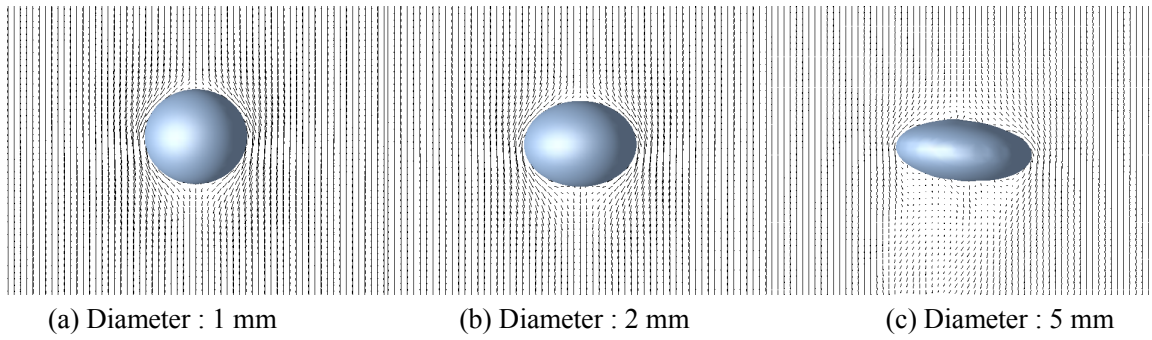


Fig. 4 Computation of a single rising bubble in water

4. DNS of a Turbulent Channel Flow containing Bubbles

4.1 Condition of Computations

A fully developed turbulent channel flow containing bubbles is investigated by the present numerical method. Before introducing the bubbles, a fully developed single-phase turbulent channel flow at the Reynolds number $Re_\tau = 180$, based on the friction velocity u_τ and a half width of the channel H , was computed. The size of the computational domain is set to $6.4H \times 2H \times 3.2H$, in the streamwise, spanwise and wall-normal directions respectively. A periodic boundary condition is used in the streamwise and spanwise directions. The x -, y - and z - axes are taken in the streamwise, wall-normal and spanwise directions respectively. The profiles of computed mean velocity and turbulence intensity agree well with the DNS results of Kim et al.⁷⁾ as shown in Figs. 5 and 6.

Computations with bubbles are initialized with the result of the single-phase flow computation. The mean pressure gradient is automatically adjusted so that the volume flow rate is kept constant. Two computations DNS-1 and DNS-2 with different surface tension coefficients are carried out for investigating the influence of the deformation of bubbles. The parameters are summarized in Table 1. The influence of the gravitational acceleration is not included in the computations. The Reynolds number $Re_\tau = 360$ corresponds to the mean velocity $U_m = 0.42m/s$ in the channel of $H = 7.5mm$ used in the experiment by Takahashi et al.⁴⁾, while assuming $D = 0.5H$, the Weber number $We = 9.2$ and $We = 37$ corresponds to and $U_m = 0.42m/s$ and $U_m = 0.85m/s$ respectively. Bubbles are suddenly introduced as shown in Fig. 7 at the non-dimensional time $t^* = u_\tau^2 t / \nu = 0$.

4.2 Results

Fig. 8 shows the time histories of the normalized wall shear stress. In the case DNS-1 the wall shear stress increases by about 20% within 100 non-dimensional time and then keeps a constant level with some fluctuation. The computation of the case DNS-2 was performed only until $t^* = 600$, when the wall shear stress reached a steady level. However, it is noted that the wall shear stress increases more gradually towards a steady level, which is slightly lower than in the case DNS-1. In the experiment by Takahashi et al.⁴⁾, the drag was reduced

Table 1. Condition of computation

		DNS-1	DNS-2
Reynolds number	$\text{Re}_\tau = 2u_\tau H / \nu$	360	360
Reynolds number	$\text{Re}_m = 2U_m H / \nu$	5500	5500
Bubble diameter	D	0.5H	0.5H
Weber number	$We = \rho U_m^2 D / \sigma$	9.2	37
Number of bubbles	N_B	54	54
Mean void ratio	α	0.086	0.086

by about 10% at the mean void ratio of 10%. The different trend in the computation may be attributed to the small Reynolds number, the large bubble size, and lack of the gravitational acceleration.

The statistics of the flow in the case DNS-2 are not shown in this paper, since the computation was stopped before the statistics converged. Fig. 9 shows the profile of the mean velocity in the case DNS-1 compared with the case without bubbles. The shapes of the profiles are similar, but the log-arithmetic region is shifted downward corresponding to the increase in the wall friction. The profiles of the turbulence intensities in the case DNS-1 and the case without bubbles are compared in Fig. 10. The peak of the streamwise component of the intensity is decreased, while the wall-normal and spanwise components are increased with the introduction of the bubbles. The decrease in the streamwise component of the intensity has also been observed experimentally by Kato et al.⁸⁾

Figs 11 and 12 show the distribution and shapes of the bubbles at $t^* = 500$ for the cases DNS-1 and DNS-2 respectively. The deformation of the bubbles is very small in the case DNS-1 due to the strong surface tension. On the other hand, significant deformation is confirmed in the case DNS-2. Bubbles near the solid walls are stretched due to the mean velocity gradient, while those near the center of the channel are almost spherical. The influence of the deformation is confirmed in the transient behavior of the wall shear stress shown in Fig. 8, but further examination of the computational results is necessary for clarifying the effect on the turbulence modulation.

5. Summary and Conclusions

A computational method for investigating the interactions between bubbles and turbulence has been developed in this study. The method employs a special front-tracking method, which tracks individual bubbles by the center positions and radius distributions. The advantage of the new method over front-capturing methods is that the interface curvature can be calculated more accurately for a given grid resolution.

This method has been applied to DNS computations of a low Reynolds number turbulent channel flow containing 54 bubbles. Contrary to the experiments, the wall shear stress is increased by about 20% at the mean void ratio of 8.6%. Supposed reasons for this qualitative difference are the large bubble size, the low Reynolds number, and the lack of the gravitational acceleration. It has been shown that turbulence intensities are strongly

modified by the introduction of bubbles. The decrease in the streamwise component of the intensity qualitatively agrees with the experiment. Although further validation of the numerical method is desired, it has been shown that the present numerical method is capable of dealing with the full interaction between bubbles and turbulence. This numerical simulation technique is expected to be a useful tool for investigating the influences of the bubble size or surface tension, since it is very difficult to control such parameters in experiments.

References

- 1) M. E. McCormick and R. Bhattacharyya, Drag reduction of a submersible hull by electrolysis, *Nav. Eng. J.*, 85:11-16, 1973.
- 2) N. K. Madavan, S. Deutsch, and C. L. Merkle, Measurements of local skin friction in a microbubble-modified turbulent boundary layer, *J. Fluid Mech.*, 156:237-256, 1985.
- 3) M. M. Guin, H. Kato, and H. Yamaguchi, Reduction of skin friction by microbubbles and its relation with near-wall bubble concentration in a channel, *J. Mar. Sci. Tech.*, 1:241-254, 1996.
- 4) T. Takahashi, A. Kakugawa, and Y. Kodama, Streamwise distribution of the skin friction reduction by microbubbles, *J. Soc. Naval Archit. Japan*, 182:1-8, 1997.
- 5) Kanai and H. Miyata, A marker-Density-Function approach for the direct numerical simulations of bubbly flows, *J. Soc. Naval Archit. Japan*, 185:21-30, 1998.
- 6) Tominaya, I. Kataoka, and T. Sakaguchi, Drag Coefficients of Bubbles (1st Report, Drag Coefficients of a Single Bubble in a Stagnant Liquid), *J. Soc. Mech. Eng. Japan*, B 61(587):2357-2364, 1995.
- 7) J. Kim, P. Moin, and R. Moser, Turbulence statistics in fully developed channel flow at low Reynolds number, *J. Fluid Mech.*, 177:133-166, 1986.
- 8) H. Kato, T. Iwashina, M. Miyanaga, and H. Yamaguchi, Effect of microbubbles on the structure of turbulence in a turbulent boundary layer, *J. Mar. Sci. Tech.*, 4:155-162, 1999.

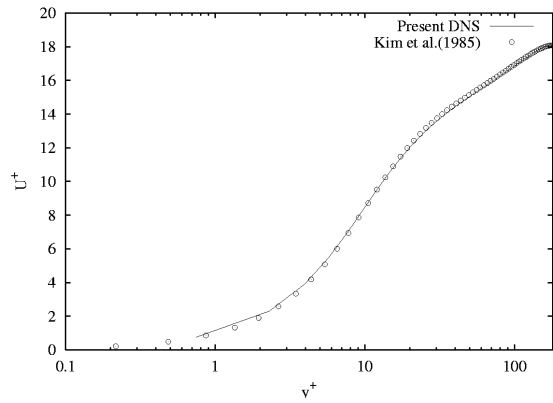


Fig 5. Mean velocity profile without bubbles

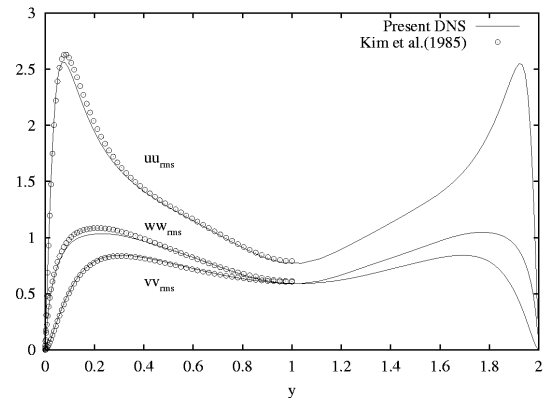


Fig 6. Turbulence intensity without bubbles

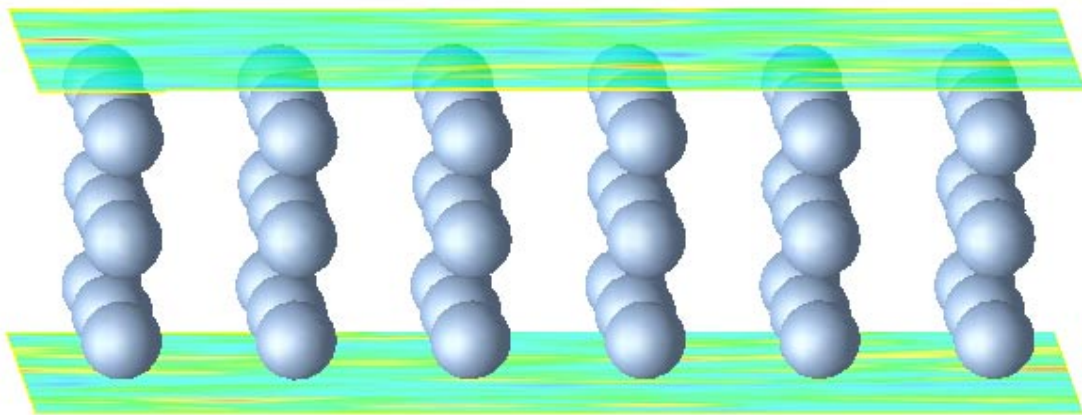


Fig. 7 Initial distribution of bubbles at $t^* = 0$

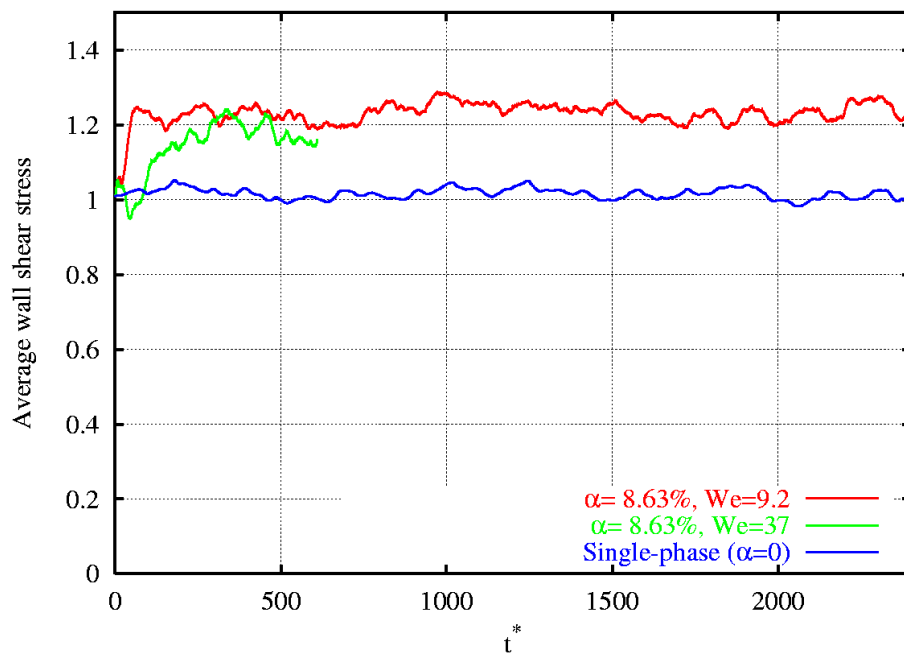


Fig. 8 Time history of the average wall shear stress

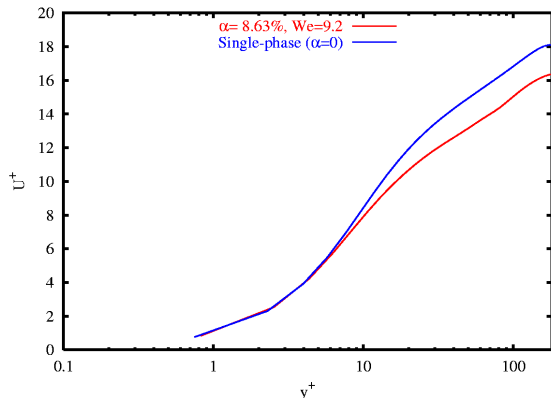


Fig. 9 Mean velocity profile

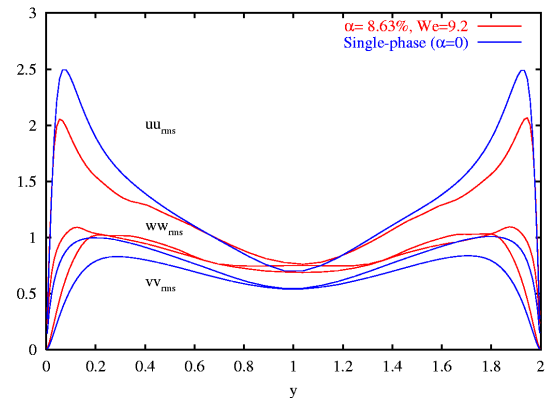


Fig. 10 Turbulence intensities

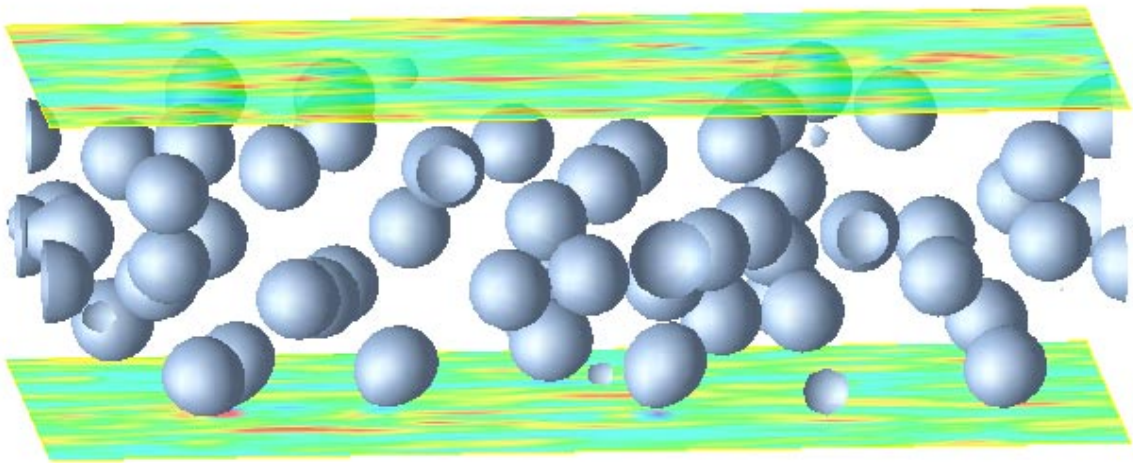


Fig 11. Distribution of bubbles in the case DNS-1 ($We = 9.4$) at $t^* = 500$. Flow is from left to right. Colors on the walls show the instantaneous shear stress.

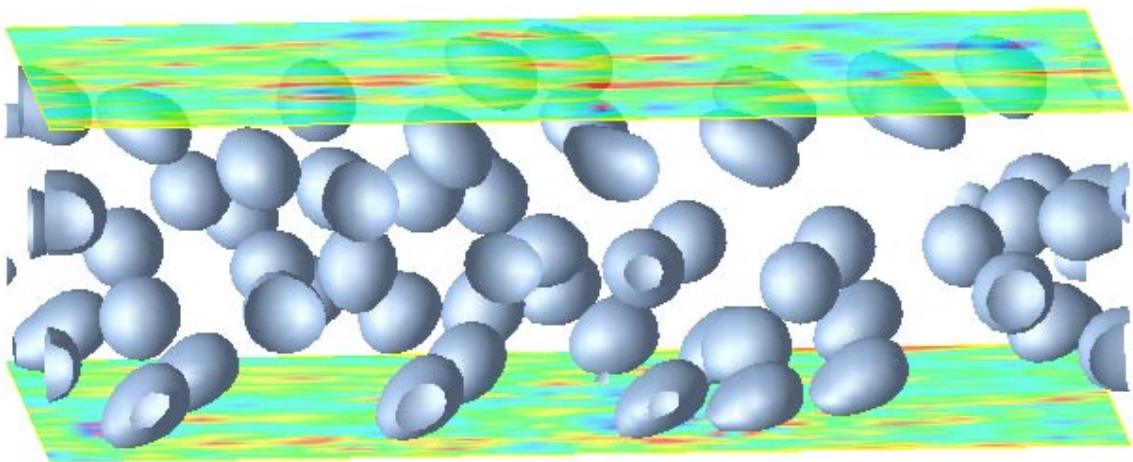


Fig 12. Distribution of bubbles in the case DNS-1 ($We = 37$) at $t^* = 500$. Flow is from left to right. Colors on the walls show the instantaneous shear stress.